

# Lab on a Chip

Accepted Manuscript



This is an *Accepted Manuscript*, which has been through the RSC Publishing peer review process and has been accepted for publication.

*Accepted Manuscripts* are published online shortly after acceptance, which is prior to technical editing, formatting and proof reading. This free service from RSC Publishing allows authors to make their results available to the community, in citable form, before publication of the edited article. This *Accepted Manuscript* will be replaced by the edited and formatted *Advance Article* as soon as this is available.

To cite this manuscript please use its permanent Digital Object Identifier (DOI®), which is identical for all formats of publication.

More information about *Accepted Manuscripts* can be found in the [\*\*Information for Authors\*\*](#).

Please note that technical editing may introduce minor changes to the text and/or graphics contained in the manuscript submitted by the author(s) which may alter content, and that the standard [\*\*Terms & Conditions\*\*](#) and the [\*\*ethical guidelines\*\*](#) that apply to the journal are still applicable. In no event shall the RSC be held responsible for any errors or omissions in these *Accepted Manuscript* manuscripts or any consequences arising from the use of any information contained in them.

Cite this: DOI: 10.1039/c0xx00000x

www.rsc.org/xxxxxx

PAPER

# On-Chip Magnetic Separation and Encapsulation of Cells in Droplets†

Aaron Chen,<sup>a</sup> Tom Byvank,<sup>a</sup> Woo-Jin Chang,<sup>b</sup> Atul Bharde,<sup>a</sup> Greg Vieira,<sup>a</sup> Brandon Miller,<sup>c</sup> Jeffrey J. Chalmers,<sup>c</sup> Rashid Bashir<sup>d</sup> and Ratnasingham Sooryakumar\*<sup>a</sup>

Received (in XXX, XXX) Xth XXXXXXXXX 20XX, Accepted Xth XXXXXXXXX 20XX

DOI: 10.1039/b000000x

Single cell study is gaining importance because of the cell-to-cell variation that exists within cell population, even after significant initial sorting. Analysis of such variation at the gene expression level could impact single cell functional genomics, cancer, stem-cell research, and drug screening. The on-chip monitoring of individual cells in an isolated environment would prevent cross-contamination, provide high recovery yield, and enable study of biological traits at a single cell level. These advantages of on-chip biological experiments is a significant improvement for a myriad of cell analyses methods, compared to conventional methods, which require bulk samples and provide only averaged information on cell structure and function. We report on a device that integrates a mobile magnetic trap array with microfluidic technology to provide the possibility of separation of immunomagnetically labeled cells and their encapsulation with reagents into pico-liter droplets for single cell analysis. The simultaneous reagent delivery and compartmentalization of the cells immediately following sorting are all performed seamlessly within the same chip. These steps offer unique advantages such as the ability to capture cell traits as originated from its native environment, reduced chance of contamination, minimal use of the reagents, and tunable encapsulation characteristics independent of the input flow. Preliminary assay on cell viability demonstrates the potential for the device to be integrated with other up- or downstream on-chip modules to become a powerful single-cell analysis tool.

## Introduction

Technological developments over the past several decades have played a major role in driving basic biology research and advancements in biomedical sciences. While cell and molecular biology techniques have laid the foundation of present diagnostics and therapeutic systems, most of these methods rely on ensemble measurements obtained from heterogeneous cell populations.<sup>1</sup> However, it has been demonstrated in different systems that even within an isogenic cell population, stochastic gene expressions exist among cells.<sup>2-5</sup> Analyzing an ensemble of cells at an individual level with high spatiotemporal resolutions can thus lead to a better understanding of such cell-to-cell variations.<sup>6</sup> Two key processes required prior to performing single-cell analyses are (i) the sorting of cells into subpopulations and (ii) the compartmentalization of these cells of interest with dedicated reagents into individually isolated environments.

### Sorting techniques

Different sorting techniques have been developed over the past decade.<sup>7-10</sup> For example, conventional flow cytometry<sup>4,11</sup> sorts cells based on their sizes and biological signatures. While it is a well-developed and commercially available technique, this approach requires expensive instrumentation. Hydrodynamic techniques<sup>12-17</sup> sort objects based on their sizes without the need for external forces or pre-labeling of biological entities. Electric-field-based techniques such as optical trap,<sup>18,19</sup>

dielectrophoresis<sup>19-23</sup> and electrokinesis<sup>24</sup> utilize the dielectric property or charge of the objects to be sorted. However, these schemes generally have strict requirements on the optical and ionic properties of the surrounding fluid, and challenges such as heating and electrolysis (bubbling) need to be addressed. In contrast, magnetic-field-based sorting, achieved by the intrinsic or extrinsic (through marker-specific magnetic bead labeling) magnetic moment of the cells,<sup>25</sup> serves as an inexpensive technique without the same difficulties that plague its electric counterparts. Schemes such as external magnets,<sup>26-32</sup> ferromagnetic channels,<sup>33</sup> ferromagnetic strips,<sup>34-36</sup> and periodic ferromagnetic patterns<sup>37,40</sup> have been shown to generate the magnetic field gradient required to manipulate magnetic objects to desired locations.

### Compartmentalizing techniques

Compartmentalization of the sorted cells of interest into individually isolated environments is a crucial step towards single-cell analysis. Various schemes have been utilized for the purpose of compartmentalization. For examples, array of wells on a proprietary chip<sup>4</sup> and microfluidic chambers<sup>41-43</sup> act as containers for single cells while delivering reagents through pumps and valves. However, the nature of these rigid confining structures limits the ability to scale up (provide as many compartments as possible) and could potentially be contaminated or worn off over multiple uses. In contrast, compartmentalization based on microfluidic droplet devices serves as an alternative

technique<sup>44-49</sup> where the containers (droplets) are created anew during the encapsulation of single cells. The number of droplets generated by the device is practically unlimited, allowing easy scale-up.

5

#### Integration of sorting and compartmentalization on a chip

In order to compartmentalize the cell while it still maintains the property as derived from the native heterogeneous environment, it is advantageous to perform the compartmentalization immediately following sorting in the same setup. However, existing work on single-cell analysis generally require transfer between instruments<sup>4</sup> or containers<sup>5</sup> from one step to another, or purification of the samples elsewhere prior to introducing them onto the compartmentalization platforms.<sup>41-43,46</sup>

<sup>49</sup> These steps could potentially lead to contamination during transfer, nonspecific loss through non-specific binding, and denaturation. While each of the chip-based sorting techniques mentioned above has its own merits, so far none has yet provided an on-chip mechanism for the compartmentalization of the sorted entities. Although sorting after compartmentalization exists in droplet microfluidics, e.g. post-encapsulation processing of droplets through hydrodynamic sorting<sup>50</sup> detection-based electric sorting<sup>46,47</sup> and droplet splitting,<sup>46,47,51</sup> unwanted effects and chemicals secreted from other cells could not be removed from the droplets through such sorting or splitting.

In this paper, we integrate for the first time, the magnetic

sorting capability of previously developed mobile magnetic trap array<sup>39</sup> immediately before the compartmentalization of cells provided by droplet microfluidics on the same device. This integration not only eliminates the steps needed between sorting and compartmentalization, but it also offers the combined advantage of low cost, biocompatibility and ease of scaling up. The rationale behind choosing mobile trap array over other chip-based sorting technologies for the integration are its

- 35 1) well-defined pick-up and drop-off locations compared to external magnet based schemes,
- 2) active separation against the flow compared to the passive ferromagnetic strips, channels or hydrodynamic sorting, and
- 3) tolerance on the ionic content of the liquid environment compared to electric field based techniques.

<sup>40</sup> These unique features couple well with the dropletization by continuously guiding magnetically labeled cells across a zero- or reverse-flow zone, leaving behind unwanted chemicals from other cells, and into an independently controlled reagent flow for <sup>45</sup> encapsulation. The streamed output of droplets containing cells separated afresh from their heterogeneous environment serves as a production line ready for further integration with other on-chip analysis techniques such as single-cell polymerase chain reaction and electrical measurements. As proof of concept, preliminary <sup>50</sup> assay on the viability of encapsulated cells through fluorescence detection was demonstrated.

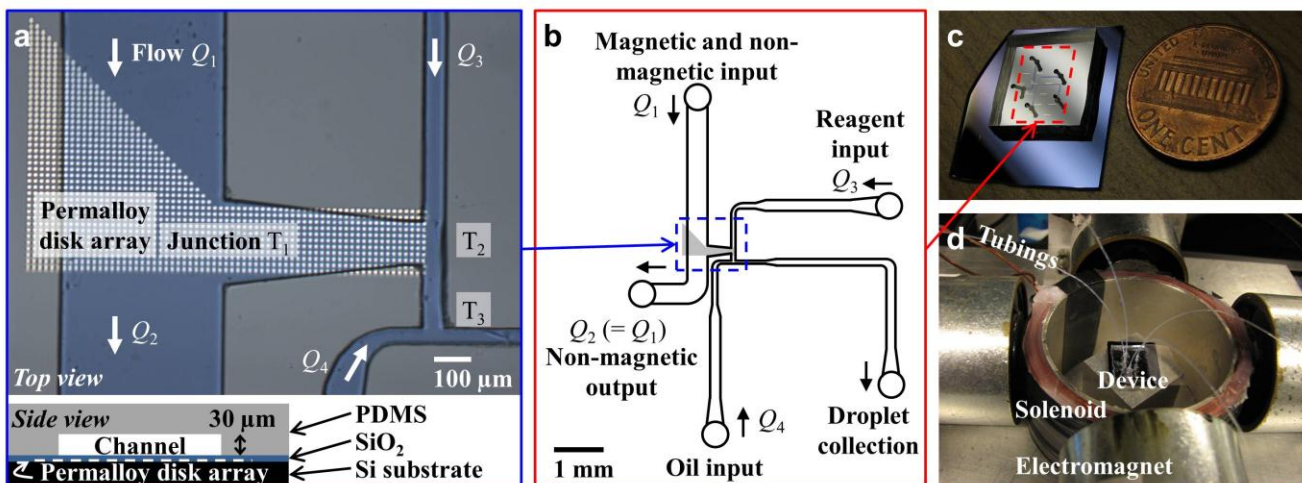


**Fig. 1** Device layout and system setup. (a) Microscope image (top) showing the channel layout on an array of permalloy ( $\text{Ni}_{0.8}\text{Fe}_{0.2}$ ) disks and a schematic side view of the device (bottom). Fluid flow rates  $Q_1$ ,  $Q_2$ ,  $Q_3$  and  $Q_4$  are indicated at corresponding channels while the three T-junctions are labeled with  $T_1$ ,  $T_2$  and  $T_3$ . (b) Schematic of full layout of the microfluidic channel. (c) Photograph of the device. (d) Photograph of the system consisting of four electromagnets and a solenoid that apply external magnetic field on the device. Tubings connected to computer-controlled syringes transfer fluid to or from the microfluidic channels of the device situated within the setup. Note the fifth tubing has not been connected yet to the droplet collection port in the picture.

## Experimental

### Device fabrication

A mask design with transparent patterns of disk arrays and microchannels was produced on a chromium-on-quartz plate (Advance Reproductions Corporation). As shown in Figure 1a, an array of permalloy ( $\text{Ni}_{0.8}\text{Fe}_{0.2}$ ) disks with 10  $\mu\text{m}$  diameter, 15  $\mu\text{m}$  centre-to-centre spacing and 84 nm height were imprinted onto a Si substrate by contact photolithography using the mask aligner

followed by sputter deposition and lift-off. A final deposition of 100 nm  $\text{SiO}_2$  on the entire surface served as a protective layer. The same photolithography was used to create microchannel molds (SU-8 2025, MicroChem) on the Si substrate. Polydimethylsiloxane (PDMS) (Dow Corning Sylgard 184) was mixed with curing agent at 10:1 ratio, poured onto the microchannel molds, cured at room temperature for 2 days, peeled from the mold, cut to desired size and punched with holes <sup>75</sup> at the end of the channels for tubing connection. The resulting PDMS channel, with layout as illustrated in Figure 1b, was

permanently bonded to the disk array substrate to form the integrated device shown in Figure 1c by the following procedure: The channel side of the PDMS as well as the  $\text{SiO}_2$  surface of the disk array were treated with UV-ozone (UVO Cleaner 42, Jelight Company Inc.) at  $\sim 1$  cm sample-lamp distance for 3 minutes, aligned and attached to each other using ethanol as a temporary lubricant in between, and then baked at  $80^\circ\text{C}$  for 30 min. To facilitate droplet formation, the channel surface was made hydrophobic prior to the experiment by treating the channel inner surface with Sigmacote (SL-2, Sigma-Aldrich) for 5~10 s followed by baking at  $110^\circ\text{C}$  for 30 min. Channel dimensions are: height 30  $\mu\text{m}$ , width of  $Q_1$  flow 400  $\mu\text{m}$ , left width of T<sub>1</sub>-T<sub>2</sub> channel 200  $\mu\text{m}$ , right width of T<sub>1</sub>-T<sub>2</sub> channel 100  $\mu\text{m}$ , length of T<sub>1</sub>-T<sub>2</sub> channel 500  $\mu\text{m}$ , width of  $Q_3$  flow 50  $\mu\text{m}$ , and narrowest width of  $Q_4$  flow 30  $\mu\text{m}$ .

## Microfluidics

Fluid flow in the microfluidic channel were remotely controlled by computer program coded in LabVIEW (LabVIEW, National Instruments Corporation), which interfaced with syringe pumps (PHD Ultra Syringe Pump, Harvard Apparatus) mounted with 25 or 50  $\mu\text{L}$  syringes (7636-01 and 7637-01, Hamilton Company). Polyethylene tubings (inner diameter 0.40 mm, 720191, Harvard Apparatus) connected between the syringes and channel ports transferred fluid to and from the microfluidic device as shown in Figure 1d. Unless otherwise noted, temperature fluctuation around the tubings was minimized (thereby stabilizing the flow) by wrapping Kimwipes (Fisher Scientific) around them and utilizing cooling fans. As there are a total of 5 ports on the channel, flow rates are controlled only at 4 ports (flow  $Q_1$ ,  $Q_2$ ,  $Q_3$  and  $Q_4$  in Figure 1a and b) through 4 individual syringe pumps; flow rate at the fifth port (droplet collection port) is given by  $Q_1 + Q_2 + Q_3 + Q_4$ . The solutions sent into or out of the channel ports are detailed below.

### 35 Magnetic and nonmagnetic input (flow $Q_1$ )

Experiments on bead separation and encapsulation were performed with a mixed magnetic and non-magnetic bead solution that contains:

- 1) 7.9  $\mu\text{m}$  diameter superparamagnetic microspheres (UMC4N/10150, Bang Laboratories, Inc.), and
- 2) 3.34  $\mu\text{m}$  diameter nonmagnetic beads (CP-30-10, Spherotech, Inc.).

Above beads were suspended in 0.1% Triton X-100 (X100, Sigma-Aldrich) at final concentrations of roughly  $1.8 \times 10^6$  and  $6.4 \times 10^6$  beads/mL for the magnetic and nonmagnetic beads respectively.

Suspension for cell experiments contained a mixture of:

- 1) Human breast cancer cells BT-474 labeled with 2.8  $\mu\text{m}$  magnetic particles (Dynabeads M-270 Streptavidin, Life Technologies Corporation) functionalized with anti-HER2 antibodies, and
- 2) red blood cells (RBCs).

These cells were suspended in phosphate buffered saline (PBS) with 5 mg/mL Pluronic F-68 (P1300, Sigma-Aldrich), 5mM ethylenediaminetetraacetic acid (EDTA) and 1% bovine serum albumin (BSA). Final cell concentrations used in separation and encapsulation experiment were roughly  $5 \times 10^5$  cells/mL (BT-474) and  $1 \times 10^5$  cells/mL (RBCs), while final concentrations

used for the cell viability experiment were  $2.5 \times 10^5$  cells/mL (BT-474) and  $2 \times 10^5$  cells/mL (RBCs). The average number of beads labeling a BT-474 cell was 1.5 with standard deviation 0.8 (out of 485 cells) after an incubation time of  $\sim 30$  min. This labeling yield could increase over time as the bead-to-cell (BT-474) ratio in solution was intentionally made higher than  $\sim 10$  beads/cell for maximum labeling.

### Non-magnetic output (flow $Q_2$ )

Although flow  $Q_2$  withdrew fluid from the microfluidic channels, a buffer solution same as that used in flow  $Q_1$  to suspend beads or cells was infused into the non-magnetic output channel (along with flows  $Q_1$ ,  $Q_3$  and  $Q_4$  from other channels) during the initial phase to fill the entire channels with fluid. After air had been removed from all the channels,  $Q_2$  was set to the desired withdrawal rate.

75

### Reagent solution (flow $Q_3$ )

Three types of solutions were used for the reagent channel, i.e. flow  $Q_3$  in Figure 1a and b, depending on the experiment conducted:

- 80 1) 0.1% Triton X-100 in de-ionized water for magnetic bead separation and encapsulation experiments,
- 2) PBS with 5 mg/mL Pluronic F-68, 5mM EDTA and 1% BSA for cell separation and encapsulation experiments, or
- 3) PBS with 1% BSA and 1.5  $\mu\text{M}$  PI (propidium iodide) for cell separation and encapsulation followed by droplet collection and fluorescence analysis of cell viability.

### The continuous phase solution (flow $Q_4$ )

Mineral oil (O121, Fisher Scientific) with 0~15% Span 80 (sorbitan monooleate, S6760, Sigma-Aldrich) as emulsifier was used as the continuous phase that surrounds the aqueous droplets.

### Droplet collection output

The output port of droplet collection channel was not connected to any tubings during the initial air-removal phase. After removal of the air and stabilization of droplet generation, a small segment (several centimeters long) of tubing was then connected to this port for the collection of droplets.

### Magnetic manipulation

100 As shown in Figure 1d, four electromagnets (OP-2025, Magnetech Corp.) and a solenoid provided in-plane ( $H_x$  and  $H_y$ ) and out-of-plane ( $H_z$ ) components of the external magnetic field:  $\mathbf{H}_{\text{ext}} = (H_x, H_y, H_z)$ . A LabVIEW program controlled the current driving the electromagnets and solenoid, allowing fields up to  $\sim 150$  Oe to be produced and remotely tuned. Magnetic trap array (local energy minima on the edges of the imprinted permalloy disks that attract magnetic objects) was mobilized with respect to the fixed disk array by application of a sequence of magnetic fields: rotation of the in-plane field, i.e.  $\mathbf{H}_{\text{ext}} = (H_1 \cdot \cos\varphi, H_1 \cdot \sin\varphi, H_z)$ ,  $\varphi = 0^\circ$  to  $180^\circ$ , followed by reversing the orientation of  $H_z$ .<sup>39</sup>

These steps resulted in the transport of magnetic beads or labeled cells around the disk periphery (e.g. from  $-x$  end to  $+x$  end) during the field rotation phase followed by its hopping to the adjacent disk (e.g. from  $+x$  end of one disk to  $-x$  end of next) when  $H_z$  was reversed. One period of the transport cycle consisted of the rotation time ( $\tau/2$ ) and wait times before ( $\tau/4$ ) and

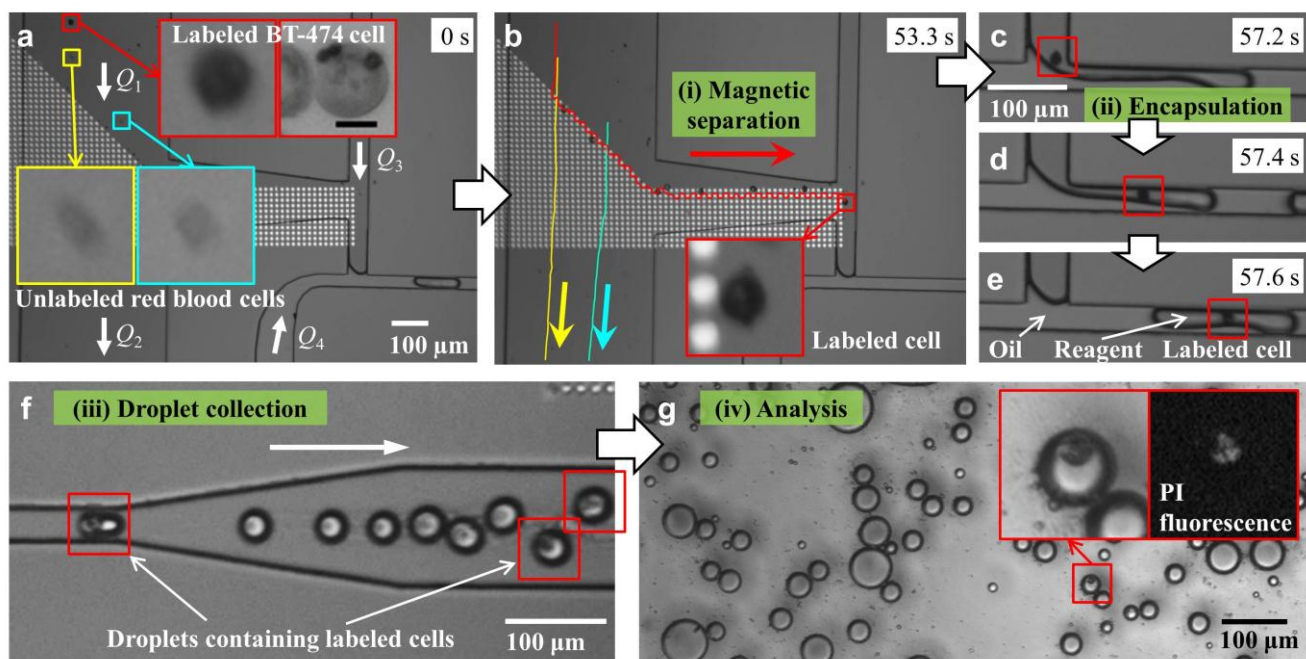


**Fig. 2** Snapshots showing the process of magnetic separation, encapsulation, droplet collection and analysis. (a) At time  $t = 0$  s, one magnetically labeled BT-474 cell and two unlabeled red blood cells are indicated by boxes and enlarged as insets, where an additional inset on the right shows a typical labeled cell in higher resolution (scale bar is  $10 \mu\text{m}$ ). The cells enter from the top left branch of the channel with flow rates  $Q_1 = Q_2 = 75 \text{ nL/min}$ ,  $Q_3 = 15 \text{ nL/min}$  and  $Q_4 = 30 \text{ nL/min}$ . (b) At  $t = 53.3$  s, movements of the three cells from  $t = 0$  s are traced with lines. The labeled cell magnetically separated to the right is indicated by the box. (c-e) Sequential snapshots taken at  $t = 57.2$ ,  $57.4$  and  $57.6$  s show the encapsulation process of the same labeled cell (indicated by the box) mixed with the reagent solution from flow  $Q_3$ . (f) Snapshot taken from a separate experiment than that of (a-e) showing droplets being transferred down the output channel. Droplets contain solution of PI (propidium iodide) at  $1.5 \mu\text{M}$  concentration, and those encapsulating labeled cells are indicated by the boxes. (g) Droplets collected from (f) are placed between a glass substrate and cover glass for detection of fluorescence signal from the PI dye. Size variation on the droplets is a result of droplet merging and breaking during the transfer step.

**Table 1** Summary of experimental parameters

Experiments	Manipulation rate $f$ (Hz)	In-plane field $H_1$ (Oe)	Flow rates (nL/min)	$Q_1$	$Q_2$	$Q_3$	$Q_4$
(i) Bead separation vs. $Q_1$	5	100	150 ~ 700	$\sim Q_1 + 10$	100	100	<sup>a</sup>
(ii) Bead separation vs. $H_1$	2	20 ~ 100	250	260	100	100	<sup>a</sup>
(iii) Bead separation vs. $f$	0.5 ~ 50	100	250	260	100	100	<sup>a</sup>
(iv) Bead encapsulation vs. $Q_1$	5	100	50 ~ 350	$Q_1$	15	30	
(v) Cell separation and encapsulation vs. $Q_1$	1	100	50 ~ 125	$\sim Q_1 + 10$	15	30	
(vi) Cell separation, encapsulation and analysis	1	100	50	$Q_1$	100	50	

<sup>a</sup> Flow not controlled.

is after  $(\tau/4)$  the inter-disk hopping was completed. The rate of transport is hence defined as  $f = 1/\tau$ , i.e. the number of disks traversed by the object per unit time. With the ratio of  $|H_z|$  to  $H_1$  set fixed at 1.5 to 1, the two central parameters for magnetic manipulation are the magnitude of the in-plane field  $|H_1|$  and the transport rate  $f$ .

### Imaging

The sequence of events was observed through an optical microscope (Leica DM2500MH) with a 10x objective lens and

recorded with a digital camera (QImaging Retiga EXi) interfaced with LabVIEW at a frame rate of 10~20 fps. The fluorescence signal from the PI dye was picked up with Leica's Texas Red Filtercube (TX2).

## Results and discussion

### Experiment overview

Magnetic and non-magnetic beads or cells were sent down the input channel at flow rate  $Q_1$  while withdrawn at a rate  $Q_2$  same

as  $Q_1$  as shown in Figure 1a and b. As an example, Figure 2a shows magnetically labeled and unlabeled cells entering the input channel on the left. While the unlabeled ones followed the flow down the channel as shown in Figure 2b, the labeled one was 5 magnetically manipulated to the far right of the disk array, mixed with the reagent flow ( $Q_3$ ), and subsequently encapsulated into a droplet with the reagent as depicted in Figure 2c-e. High purity can be achieved, prohibiting unlabeled cells into the separation channel between junctions  $T_1$  and  $T_2$ , by increasing  $Q_2$  slightly 10 ( $\sim 10$  nL/min) higher than  $Q_1$ . As a preliminary viability assay on the encapsulated cells, the droplets were transferred down the output channel (Figure 2f), collected in a tubing and then re-dispersed onto a glass substrate for the fluorescence detection of PI (propidium iodide) inside the encapsulated cells (Figure 2g). 15 Video 1 and Video 2 in the Electronic Supplementary Information show the process of separation and encapsulation of magnetic beads and labeled cells. Table 1 lists all the experiments conducted in this work and the respective parameters used.

### Quantification of device performance with magnetic beads

#### 20 Separation efficiency

Separation of targeted magnetic entities is achieved by the sequence of external magnetic fields (described in the Experimental Section). An important parameter characterizing separation efficiency of the device is defined by:

$$25 \quad \gamma_{\text{object}} = \frac{\text{number of object separated to junction T}_2}{\text{number of object entering the disk array}} \quad (1)$$

where *object* can be magnetic beads or labeled cells. In this study magnetic and nonmagnetic bead solutions (Experimental Section) were used to evaluate  $\gamma_{\text{bead}}$ . The smaller nonmagnetic bead (3.4  $\mu\text{m}$ ) compared to the magnetic bead (7.9  $\mu\text{m}$ ) allowed 30 visualization of the flow and distinguishability between the two types of beads. Based on prepared bead concentration, we found the recovery rate of magnetic beads entering the disk array to be 58% as some beads may settle on tubing surface. As summarized in Figure 3, the influence of the input flow rate  $Q_1$ , in-plane magnetic field strength  $H_1$  ( $|H_z| = 1.5 H_1$ ) and transport rate  $f$  on the separation efficiency  $\gamma_{\text{bead}}$  were investigated.

For fixed  $H_1 = 100$  Oe and  $f = 5$  Hz, Figure 3a depicts that high separation efficiency ( $\gamma_{\text{bead}} > 90\%$ ) was maintained until the input flow rate  $Q_1$  exceeds  $\sim 300$  nL/min. Beyond this threshold,  $\gamma_{\text{bead}}$  40 steadily decreases to less than 10% at  $Q_1 \geq 600$  nL/min. As an increasing hydrodynamic drag force could account for the decrease in  $\gamma_{\text{bead}}$ , we estimate the force required to detach a bead, with typical magnetic susceptibility of 0.1 (see footnote‡), off the magnetic trap to be  $\sim 100$  pN. This corresponds to a flow rate of 45  $Q_1 = 970$  nL/min based on Stokes law (neglecting near-wall effects). However, the observed flow rate at which  $\gamma_{\text{bead}}$  starts decreasing from its high value of  $> 90\%$  is  $\sim 300$  nL/min, which is much lower than the estimated flow rate (970 nL/min). Our observation suggests other explanations for the decrease in  $\gamma_{\text{bead}}$  50 as  $Q_1$  increases: Higher  $Q_1$  results in

- 1) higher bead throughput and therefore fewer vacant disks on the array to accommodate incoming beads into the  $T_1$ - $T_2$  channel,
- 2) less time for beads floating above the array surface to be 55 pulled towards the disks by the magnetic trapping force or

gravity, and

- 3) possibility for the bead to miss the next disk during the hopping phase of magnetic manipulation.

As expected, Figure 3b illustrates that a greater magnetic field 60 strength ( $H_1$ ) results in an enhanced magnetic force and therefore higher  $\gamma_{\text{bead}}$  for a given flow rate  $Q_1$  and transport rate  $f$ .

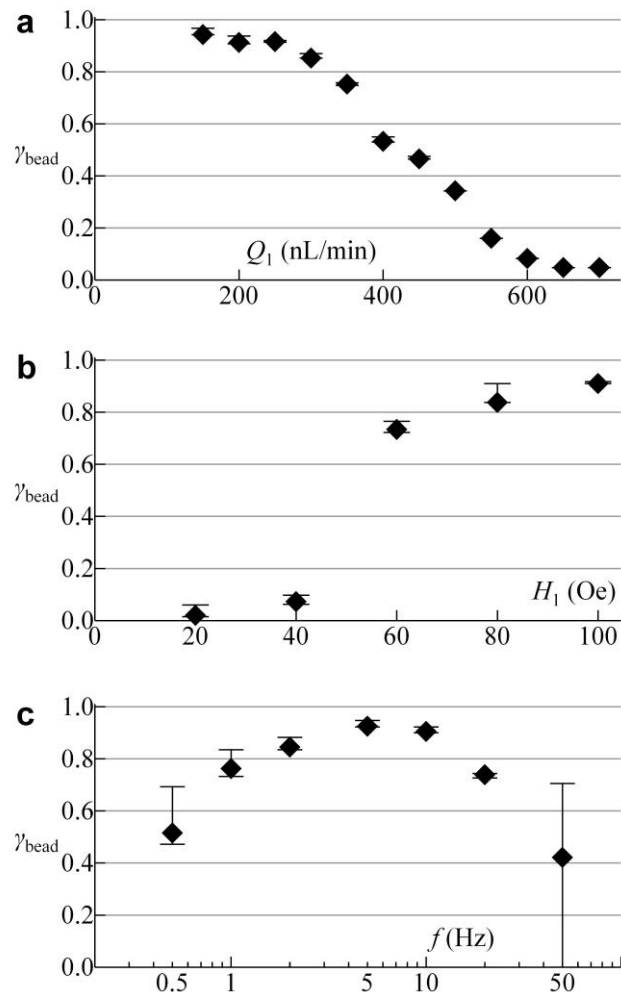


Fig. 3 Quantification of the separation efficiency  $\gamma_{\text{bead}}$  for 7.9  $\mu\text{m}$  diameter magnetic beads.  $\gamma_{\text{bead}}$  is plotted as a function of (a) input flow rate  $Q_1$ , (b) 65 in-plane field strength  $H_1$  and (c) rate of transport  $f$ , corresponding to experiments (i), (ii) and (iii) in Table 1 respectively. Data points (filled diamonds) are based on measured number of separated magnetic beads over a single run of experiment for each plot. Vertical bars at the data points represent the effect of flow fluctuation discussed in the text (not 70 measurement errors). The number of magnetic beads counted range from 200 to 450, yielding an estimated statistical error of  $\sim 200^{1/2}/200 = 7.1\%$  due to finite sample size.

Figure 3c illustrates that increasing the transport rate  $f$  while keeping other parameters fixed yielded more effective separation 75 for  $f$  up to  $\sim 5$  Hz. In this case, rapid transport of the beads into the separation channel yielded more vacant disks to accommodate incoming beads, hence the increase in  $\gamma_{\text{bead}}$  for  $f$  in the range of 80 0.5 to 5 Hz. Transport rates higher than 5 Hz become less effective at separation since (i) motion of the trap against the flow ( $Q_1$ ) during the field rotation cycle decreases the minimum flow rate required to detach the bead from 970 nL/min ( $f = 5$  Hz) to 480 nL/min ( $f = 25$  Hz) and to zero ( $f = 50$  Hz) according to

calculation, and (ii) too short a wait time ( $\tau/4 < 10$  ms) during the inter-disk hopping phase may result in stalling (inability to hop to the next disk) of the bead. The optimal manipulation rate of  $f = 5$  Hz implies a maximum separated bead throughput of about 30 beads/s, assuming that all the disks ( $\sim 6$  rows) are outputting beads into junction  $T_2$  at a maximum occupancy with 1 bead per disk. This yielded an estimate on the maximum bead concentration for effective separation to be  $\sim 7.2 \times 10^6$  beads/mL for  $Q_1 = 250$  nL/min. Though this limitation on the separation throughput is an inherent property of the manipulation scheme, increasing the number of rows of the disk array could potentially enhance the throughput.

We found that flow fluctuation due to temperature variation (from heat generated from the electromagnets) around the tubing plays an important factor in separation efficiency. In the experiments performed in Figure 3, i.e. (i), (ii) and (iii) in Table 1, thermal insulation was not applied on the tubings, and the amount of fluid flowing unwantedly in the  $T_1$ - $T_2$  channel ranged from none (when the electromagnets had not been turned on) to about 7 nL over a time scale of 10 s (maximum fluctuating flow rate of  $\sim 40$  nL/min) after extended use of the electromagnets ( $\sim 1$  hour). The effect of such flow fluctuation on the separation efficiency is best reflected by the vertical bars drawn on the data points in Figure 3: The upper bound of the vertical bar on the data point takes into account magnetic beads that were successfully separated into the  $T_1$ - $T_2$  channel but pushed off into the nonmagnetic output channel due to flow fluctuation; similarly, the lower bound is set by excluding magnetic beads that were pushed into the  $T_2$ - $T_3$  channel by flow fluctuation without being magnetically manipulated. The observed flow fluctuation was able to occasionally overcome the reverse flow of  $Q_2 - Q_1 = 10$  nL/min at the  $T_1$ - $T_2$  channel to have a significant impact on the separation efficiency under very high and very low manipulation rates as depicted by the large vertical bars at  $f = 0.5$  Hz and  $f = 50$  Hz in Figure 3c. This can be reasoned as the following: At very low  $f$ , manipulation rate cannot keep up with the bead input, and the disk array is jammed with magnetic beads such that those untrapped are easily pushed by flow fluctuation; at very high  $f$ , stalled magnetic beads (discussed earlier) are easily knocked off or pushed forward by flow fluctuation. Flow stabilization by thermal insulation on the tubings (Experimental Section) was applied for the experiments in the later sections, i.e. (iv), (v) and (vi) in Table 1, where the fluctuation was reduced to much less than 10 nL/min to facilitate the low-rate encapsulation process.

Due to the huge parameter space available for exploration, we will qualitatively discuss other factors that could affect the separation efficiency. For examples, the higher placement of the disk array with respect to the channel in Figure 1a compared to the lowered one in Figure 2a allows greater chance of the magnetic objects to be separated into channel  $T_1$ - $T_2$ , but it may also cause piling up of these objects as they hit the tilted upper channel wall if the objects tend to stick. Same device was used within each set of experiment, and the quantitative effect of different disk array-channel alignments on the separation efficiency is not investigated here.

The size of the magnetic beads was chosen to be comparable to that of the disk size and gap. Much smaller beads are oversensitive to localized fields and may not be able to hop from

one disk to the next, whereas oversized beads average out the energy landscape to experience little manipulation force compared to the drag force.

To summarize, achieving high separation efficiency for the magnetic beads used in this device requires:

- 1) low input flow rate ( $Q_1 < 250$  nL/min),
- 2) high field strength ( $H_1 > 100$  Oe),
- 3) optimal manipulation rate ( $f \sim 5$  Hz),
- 4) low bead concentration ( $< 7.2 \times 10^6$  beads/mL),
- 5) optimal bead size (comparable to disk size and spacing),
- 6) thermally insulated tubing, and
- 7) optimal disk array shape and position for increased accommodation in channel  $T_1$ - $T_2$  while avoiding piling up.

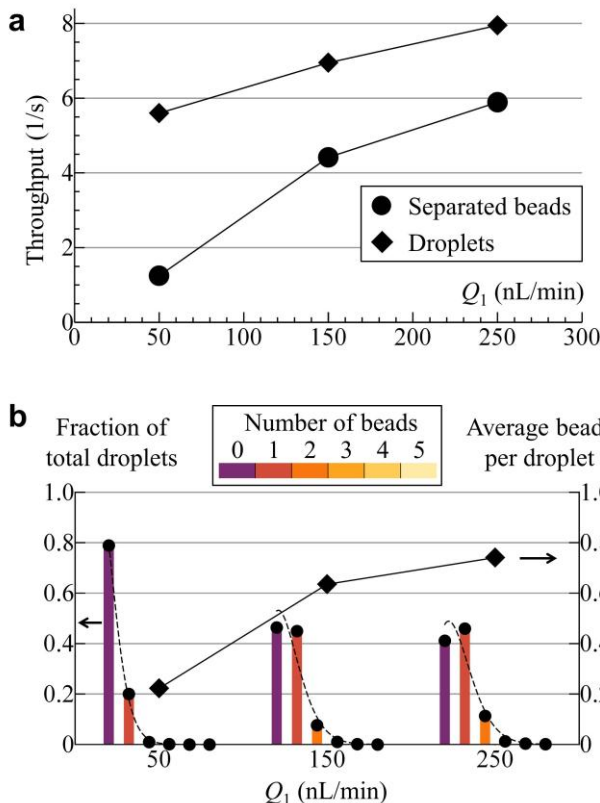


**Fig. 4** Quantification of the encapsulation characteristics with  $7.9 \mu\text{m}$  diameter magnetic beads. (a) Separated bead (filled circles) and droplet (filled diamonds) throughputs as a function of input flow rate  $Q_1$ . Experimental parameters are given by (iv) in Table 1. (b) Extracted from the same experiment as in (a), fraction of droplets (corresponding to the left vertical axis) containing various number of beads are plotted as dots with underlying color-coded bars at flow rates  $Q_1 = 50, 150$  and  $250$  nL/min. Dashed curves at each  $Q_1$  represent Poisson distribution function (Equation (2)) with mean value  $\lambda$  set by the measured average number of beads per droplet (plotted as filled diamonds with values corresponding to the right vertical axis). Total number of droplets taken into account ranges from 840 to 1251, and an estimate on the statistical deviation due to finite sample size is  $\sim 840^{1/2}/840 = 3.5\%$ .

#### Separation purity

Purity of separation is defined as the ratio of number of nonmagnetic objects entering the nonmagnetic output channel (flow  $Q_2$ ) to that of the total number of nonmagnetic objects entering the disk array. We found two major factors contributing to the purity:

- 1) the amount of reverse flow ( $Q_2 - Q_1$ ) at channel  $T_1$ - $T_2$ , and

2) the amount of flow fluctuation.

Under a fixed reverse flow of  $Q_2 - Q_1 = 10$  nL/min, purity was found to be 100% with stabilized flow but 98% when without, as flow fluctuation (discussed in the previous subsection) could occasionally overcome the reverse flow. For zero reverse flow ( $Q_1 = Q_2$ ), purity was found to be 96% even with stabilized flow. Each of the percentages above were obtained through counting >500 nonmagnetic beads.

#### 10 Encapsulation characteristics

To quantify the encapsulation aspect of the device, the same magnetic bead solution described above (see Experimental Section) is used. As shown in Figure 4a, droplet throughput, i.e. droplet generation rate, is maintained at 5–8 droplets per second, while the separated bead throughput (entering the dropletization junction  $T_3$ ) is varied from 1 to 6 beads per second by tuning the input flow rate  $Q_1$  (note  $Q_2$  is set equal to  $Q_1$ ). This feature enables the number distribution of magnetic beads encapsulated within the droplets to be manipulated as shown in Figure 4b.

20 The encapsulation can be approximated as discrete independent events that occur randomly in time. The probability for a droplet to encapsulate  $k$  beads is given by the Poisson distribution function  $P(k)$ .<sup>52</sup>

$$P(k) = \lambda^k e^{-\lambda} / k! \quad (2)$$

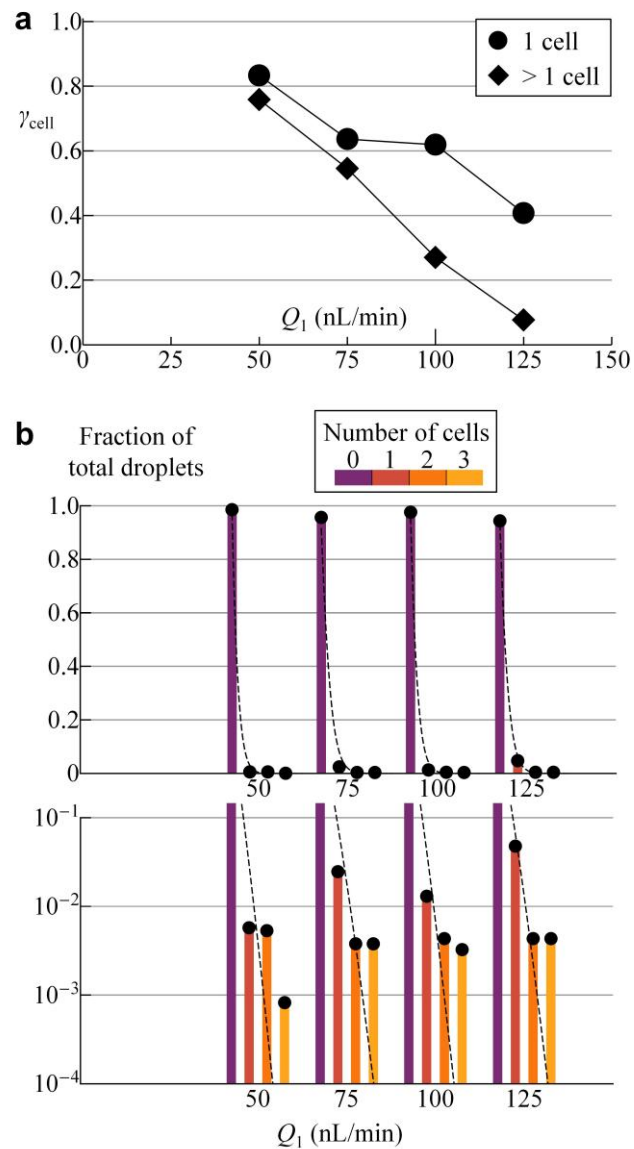
25 where  $\lambda$  is the mean of  $P(k)$ , i.e. average number of beads per droplet. It has long been a challenge in microfluidic-based approaches to overcome the inherent Poisson statistics in typical encapsulation processes and to achieve single-cell encapsulation.<sup>53,54</sup> As an example of the limitation imposed by 30 Poisson statistics, taking the derivative of Equation (2) with respect to  $\lambda$ , one finds that the percentage of single-object droplets can be maximized to  $P(1) = 36.8\%$  at  $\lambda = 1$ ; however, this is accompanied by a comparable number of empty droplets (also 36.8%) and multi-object droplets (26.4%). On the other 35 hand, reducing  $\lambda$  (average number of objects per droplet) could increase the ratio of single- to multi-object droplets but at the expense of having a large fraction of empty droplets, e.g. at  $\lambda = 0.1$ ,  $P(1)/(P(2) + P(3) + P(4) + \dots) = 9.0\% / 0.47\% \approx 19$  but  $P(0) = 90.5\%$ .

40 Figure 4b illustrates that the number distribution of beads in a droplet at each flow rate  $Q_1$  largely follow Poisson distribution based on the measured average number of beads per droplet. Interestingly, the fraction of single-bead droplets in our study exceeds that imposed by Poisson statistics by a small yet 45 observable amount of ~11% (greater than the estimated statistical error of 3.5%) at  $Q_1 = 150$  and 250 nL/min in Figure 4b. We attribute this to the fact that at higher throughput, i.e. shorter bead-to-bead distance, a rotating magnetic field with  $|H_2|/H_1 = 1.5$  results in repulsive dipolar interactions between the beads 50 travelling from junction  $T_2$  to  $T_3$ , causing them to self-arrange into a more evenly spaced configuration before being encapsulated. This feature increases the fraction of single-bead droplets. Increasing the length of channel  $T_2$ – $T_3$  could potentially further enhance the fraction of single-bead droplets.

#### 55 Separation and encapsulation of labeled cells

A heterogeneous mixture of labeled BT-474 and unlabeled red

blood cells (RBCs) described in the Experimental Section served as a sample solution to demonstrate the separation-encapsulation



60 **Fig. 5** Separation efficiency ( $\gamma_{cell}$ ) and encapsulation characteristics of labeled BT-474 cells. (a)  $\gamma_{cell}$  is plotted as a function of input flow rate  $Q_1$ . Experimental parameters are given by (v) in Table 1. Each cell aggregate is counted as one entity, where single-cell (filled circles) and multi-cell (filled diamonds) entities are plotted separately. Total cell entity counts 65 range from 33 to 58 for each  $Q_1$ , and the estimated statistical error due to finite sample size is  $\sim 33^{1/2}/33 = 17\%$ . (b) Extracted from the same experiment as in (a), fraction of droplets containing various number of cells are plotted as dots with underlying color-coded bars at flow rates  $Q_1 = 50, 75, 100$  and  $125$  nL/min. Bottom plot is a log-scaled plot with 70 droplet fraction ranging from  $10^{-4}$  to  $10^{-1}$ . Dashed curves at each  $Q_1$  represent Poisson distribution function with mean value  $\lambda$  set by the measured average number of cells per droplet. Total number of droplets taken into account ranges from 230 to 2400, and an estimate on the statistical deviation due to finite sample size is  $\sim 230^{1/2}/230 = 6.6\%$ .

75 function of the device. RBCs were chosen as unlabeled cells due to their lack of HER2 expression and the distinctive smaller sizes compared to the labeled BT-474 cells, offering visualization on the flow. Other cell types or concentrations are not investigated in

this paper but could potentially be used in the device, provided they do not adhere to surfaces of the channel or disk array to hinder device function. Based on prepared concentration, recovery rate of the labeled cells used in this study entering the disk array was found to be 39% since cells have a higher tendency to adhere to tubing surface. A high separation purity of 100% (out of >1200 red blood cells) was achieved with flow stabilization and reverse flow at channel T<sub>1</sub>-T<sub>2</sub> (see discussion in previous section). As shown in Figure 5a, due to the lower magnetic moment of the labeling particle, larger cell size and propensity to aggregate, the optimal flow rate to achieve efficient separation of the cells ( $\gamma_{cell} > 75\%$ ), was at  $Q_1 < 50$  nL/min while the optimal transport rate was  $f \sim 1$  Hz. Both the size and shape of the cells or aggregates affect the separation efficiency. Non-aggregating or smaller single cells have a higher  $\gamma_{cell}$  than aggregates or larger cells due to smaller fluid drag force; linear chain-shaped aggregates tend to orient parallel to the flow direction and thereby experience less drag force when compared to round-shaped aggregates. Although the number of beads attached per cell (labeling yield) was maximized for optimal separation, it differed from cell to cell (Experimental Section) due to the amount of receptors present on cell surface; higher labeling yield could increase the magnetic force for a given cell size and therefore higher separation efficiency. To summarize, the marker-specific separation scheme presented here is also selective based on variation of cell size, shape and extent of cell aggregation as well as the amount of receptors expressed per cell.

Encapsulation of labeled cells proves to be fundamentally different from encapsulating magnetic beads. The reduced flow rate for effective separation, tendency of cell aggregation and adhesion to surfaces lowers the separated cell throughput to below 0.15 cells per second and an average of lower than 0.1 cells per droplet at flow rates of  $Q_1 = 50 \sim 125$  nL/min. Although at such a low  $\lambda$  value of 0.1, Poisson statistics predicts a high single-cell to multi-cell droplet ratio of 19 (see previous section), the observed difference between single-cell and multi-cell droplet fractions still falls within an order of magnitude as depicted in Figure 5b. This can be understood from the assumption of the encapsulation process as independent random events in Poisson statistics – a feature that becomes less valid due to the tendency for a cell to carry other cells into the same droplet through aggregation. As shown in Figure 5b, measured multi-cell droplet fractions are indeed higher than those predicted by the Poisson distribution functions  $P(k)$  ( $k = 2, 3$ ), whereas measured single-cell droplet fractions are lower than  $P(1)$  at corresponding flow rates. Such deviation from Poisson statistics may offer opportunities for investigating the probability of time-correlated events and insights on cell-cell interaction.

While high throughputs have been achieved in existing chip-based sorting techniques (e.g.  $\sim 10^4$  cells/s with dielectrophoresis<sup>23</sup> and  $>10^5$  cells/s with ferromagnetic strips<sup>34</sup>) and microfluidic encapsulation devices ( $>100$  droplets/s<sup>46-49</sup>), the novelty of the work presented here lies not in achieving high throughput of cells or droplets but rather the coupling of the two; challenges such as flow stability exist at low rather than high droplet generation rates. The ability of the presented device to down-tune droplet generation rate below 10 Hz to match with the low separated cell throughput has the advantages of increased

single-cell droplet fraction, minimized reagent consumption and reduced chance of cell rupture due to strong shear flow. This feature of coupling a large input flow of cells to a slow dropletization is particularly suitable for the processing of rare cells.

### Preliminary cell staining and viability assay

The unique channel layout of the device shown in Figure 1 opens up a broad range of downstream applications after the encapsulation of selected cells. The reagent flow ( $Q_3$ ) from the branch channel (Figure 1b) not only draws the separated magnetic object from junction T<sub>2</sub> to T<sub>3</sub>, thereby facilitating the encapsulation process, it also offers several advantages:

- 1) Separated objects enter a fresh chemical environment of the reagent several seconds before encapsulation, reducing contamination from the non-separated objects and degradation of the reagent over time.
- 2) Minimal use of the reagent, i.e. all fluid from flow  $Q_3$  (except a slight reverse flow into channel T<sub>1</sub>-T<sub>2</sub>) is encapsulated in the droplet.
- 3) Different surface chemistries can be introduced via flow  $Q_1$  than to  $Q_3$ . For example, while a hydrophilic surfactant is desirable in  $Q_1$  as it reduces cell adhesion to the surface, it hinders the stability of water-in-oil droplets if encapsulated. The reagent channel therefore allows the chemistry surrounding the separated cells to be switched from adhesion-prevention (with 5 mg/mL Pluronic F-68 surfactant) to droplet-friendly solvent (no surfactant).

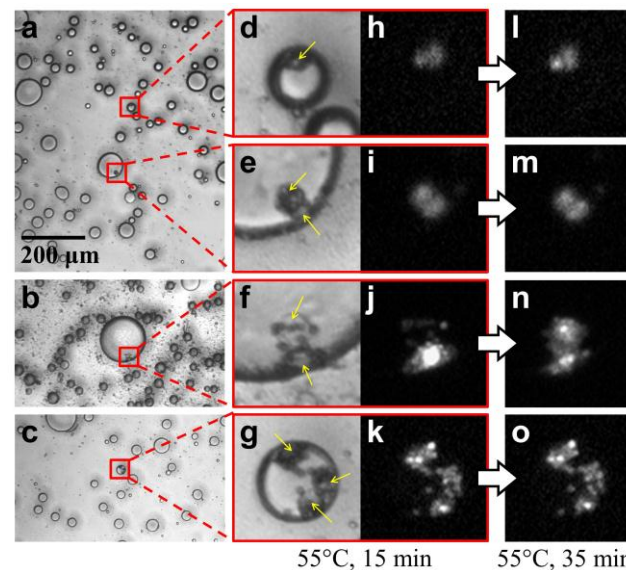


**Fig. 6** Cell viability detection with PI (propidium iodide) fluorescence of the encapsulated cells at 55°C. (a-c) Droplets (appearing as circles ranging between 10  $\mu$ m and 150  $\mu$ m in diameter) surrounded by mineral oil solution as the continuous phase are placed between a glass substrate and cover glass, and heated at 55°C for 15 min. Photographs of four droplets encapsulating labeled BT-474 cells (indicated by the arrows) are enlarged (d-g) with their respective fluorescence images (h-k) of the PI dye. (l-o) Fluorescence images taken at 35 min after heating.

As a proof of concept, Figure 6 demonstrates a preliminary assay on the viability of encapsulated cells at a raised temperature of 55°C by utilizing the reagent channel to transfer PI dye. PI is generally excluded outside the membrane by live cells, and since

the fluorescence intensity of PI increases by many fold when it enters a dead cell to bind with nucleic acids, it serves as an indicator of cell viability. 31 labeled BT-474 cells were observed to be magnetically separated from red blood cells and 5 encapsulated in droplets containing PI within the presented device using parameters given by (vi) in Table 1. Due to the difficulty in processing small amount of droplets with this preliminary method,  $Q_3$  and  $Q_4$  were increased for more droplets. Subsequent collection of the droplets in the tubing and re-10 dispersion onto a glass substrate mounted with a cover glass allowed for preservation and ease of observation as shown in Figure 6a-c. Though these transferring steps resulted in large shear flow that merged and broke about 33% of droplets into larger and smaller sizes, four droplets containing 1, 2, 2 and 3 15 cells were observed (Figure 6d-g), yielding a recovery rate of  $8/31 \approx 26\%$  from the device. Prior to and within the first 25 min of heating at 55 °C, only 1 out of the 8 encapsulated cells appeared to be alive based on their PI fluorescence retention as 20 shown in Figure 6h-k. After 35 min of heating, the fluorescence image shown in Figure 6l-o compared to those in Figure 6h-k indicates eventual death of the one live cell (top cell in Figure 6f). Both the recovery rate (~26%) and portion of recovered live cells (~12.5%) were not ideal in this preliminary assay. However, we believe that through integration with suitable on-chip observation 25 platforms after the encapsulation step, the device has the potential to offer high recovery yield of live cells and allow detection on cell-to-cell variation with high spatiotemporal resolution.

### Potential modules for integration

We envision other useful experimental modules that could be 30 integrated with the separation and encapsulation functionalities of the device:

- 1) Analysis techniques such as single-cell PCR (polymerase chain reaction) for the amplification and detection of rare biological signatures of individual cells could be realized by 35 introducing temperature zones on the microfluidic channels.
- 2) Electrical measurement could be performed by replacing mineral oil with, for example, the conductive ionic liquid for determining properties as the conductance or stiffness of the cell or detecting the change in surrounding solvent.
- 3) On-chip labeling, upstream of separation, through properly 40 designed channels to mix the functionalized magnetic particles with cells would reduce the preparation time and amount of reagent needed for the immunomagnetic labeling of targeted cells.
- 4) Overcoming the Poisson statistics of encapsulation by 45 incorporating real-time feedback on the rate of transport ( $f$ ): By monitoring the traffic of magnetic objects in channels T<sub>1</sub>-T<sub>2</sub> and T<sub>2</sub>-T<sub>3</sub>, one could achieve a more uniform throughput of separated objects and thus encapsulating a more consistent 50 number of objects per droplet.

### Conclusions

We have presented a scheme which integrates mobile magnetic trap array with droplet microfluidics that allows on-chip separation of magnetically labeled cells from a heterogeneous 55 population, immediately followed by the encapsulation of these cells into droplets with the reagents. The portable device can be

fabricated at low cost and requires small (~microliters) fluid volumes, thereby permitting fast processing and solution analysis. With the remote, programmable and simultaneous transport on 60 multiple cells, we demonstrated separation of breast cancer cell line (BT-474) with greater than 75% separation efficiency under optimal flow rates and 100% purity (no unlabeled cells were encapsulated), achieved by flow stabilization and the active magnetic separation against a reverse flow. Preliminary cell 65 viability assay subsequent to encapsulation was also demonstrated, permitting analysis on a single-cell basis rather than averaging properties over bulk populations. This separation-encapsulation functionality could become a key component in future single-cell analysis platforms with prospect to impact 70 biomedical applications, cancer research, stem cell biology and immunology.

### Acknowledgements

A.C. thanks H.-C. Chung and K. Kwak for advice on fabrication of the device and B. Yu, X.-M. Wang and J.-Y. Ma for help on 75 cell culturing. R.S. acknowledges funding from the U.S. Army Research Office under contract W911NF-10-1-0353. R.S., J.J.C. and R.B. acknowledge the support of the NSF NSEC at OSU grant number EEC-0914790.

### Notes and references

<sup>80</sup> <sup>a</sup> Department of Physics, The Ohio State University, Columbus, Ohio, 43210, USA.  
 E-mail: [soory@mps.ohio-state.edu](mailto:soory@mps.ohio-state.edu)

<sup>b</sup> Department of Mechanical Engineering and School of Freshwater Sciences, University of Wisconsin-Milwaukee, Milwaukee, Wisconsin, 53201, USA.

<sup>c</sup> William G. Lowrie Department of Chemical and Biomolecular Engineering, The Ohio State University, Columbus, Ohio, 43210, USA.

<sup>d</sup> Department of Electrical and Computer Engineering, Bioengineering, Micro and Nanotechnology Laboratory, University of Illinois at Urbana-Champaign, Urbana, Illinois, 61801, USA.

† Electronic Supplementary Information (ESI) available: Video 1: Separation of magnetic beads from non-magnetic beads followed by encapsulation into droplets. Video 2: Separation of immunomagnetically labeled BT-474 from unlabeled red blood cells followed by encapsulation 95 into droplets. See DOI: 10.1039/b000000x/

‡ Based on susceptibility measurement on 8.18  $\mu\text{m}$  diameter beads from the same company (UMC4F/9560, Bang Laboratories, Inc.) and scaling by the ratio between their magnetic contents, 4%:2.4%.

<sup>100</sup> 1 K. J. Skojoerbo, *Anal. Chem.*, 1995, **67**, 449.  
 2 M. B. Elowitz, A. J. Levine, E. D. Siggia and P. S. Swain, *Science*, 2002, **297**, 1183.  
 3 S. V. Avery, *Nat. Rev. Microbiol.*, 2006, **4**, 577.  
 4 P. Dalerba, T. Kalisky, D. Sahoo, P. S. Rajendran, M. E. Rothenberg, 105 A. A. Leyrat, S. Sim, J. Okamoto, D. M. Johnston, D. Qian, M. Zabala, J. Bueno, N. F. Neff, J. Wang, A. A. Shelton, B. Visser, S. Hisamori, Y. Shimono, M. van de Wetering, H. Clevers, M. F. Clarke and S. R. Quake, *Nat. Biotechnol.*, 2011, **29**, 1120.  
 5 A. A. Powell, A. H. Talasaz, H. Zhang, M. A. Coram, A. Reddy, G. Deng, M. L. Telli, R. H. Advani, R. W. Carlson, J. A. Mollick, S. Sheth, A. W. Kurian, J. M. Ford, F. E. Stockdale, S. R. Quake, R. F. Pease, M. N. Mindrinos, G. Bhanot, S. H. Dairkee, R. W. Davis and S. S. Jeffrey, *PLoS One*, 2012, **7**, e33788.  
 6 F. S. O. Fritzsch, C. Dusny, O. Frick and A. Schmid, *Annu. Rev. Chem. Biomol. Eng.*, 2012, **3**, 129.  
 7 C. Yi, C.-W. Li, S. Ji and M. Yang, *Anal. Chim. Acta*, 2006, **560**, 1.  
 8 S. Ishii, K. Tago and K. Senoo, *Appl. Microbiol. Biotechnol.*, 2010, **86**, 1281.

9 A. A. Bhagat, H. Bow, H. W. Hou, S. J. Tan, J. Han and C. T. Lim *Med. Biol. Eng. Comput.*, 2010, **48**, 999.

10 A. Lenshof and T. Laurell, *Chem. Soc. Rev.*, 2010, **39**, 1203-1217.

11 K. Ohnuma, T. Yomo, M. Asashima and K. Kaneko, *BMC Cell Biology*, 2006, **7**, 25.

12 L. R. Huang, E. C. Cox, R. H. Austin and J. C. Sturm, *Science*, 2004, **304**, 987-990.

13 M. Yamada, M. Nakashima and M. Seki, *Anal. Chem.*, 2004, **76**, 5465-5471.

14 M. Yamada and M. Seki, *Lab Chip*, 2005, **5**, 1233-1239.

15 S. Choi, S. Song, C. Choi and J.-K. Park, *Lab Chip*, 2007, **7**, 1532-1538.

16 A. A. S. Bhagat, S. S. Kuntaegowdanahalli and I. Papautsky, *Lab Chip*, 2008, **8**, 1906-1914.

17 Z. G. Wu, B. Willing, J. Bjerketorp, J. K. Jansson and K. Hjort, *Lab Chip*, 2009, **9**, 1193-1199.

18 X. Wang, S. Chen, M. Kong, Z. Wang, K. D. Costa, R. A. Li and D. Sun, *Lab Chip*, 2011, **11**, 3656.

19 K. Morishima, F. Arai, T. Fukuda, H. Matsuura and K. Yoshikawa, *Anal. Chim. Acta*, 1998, **365**, 273.

20 F. F. Becker, X.-B. Wang, Y. Huang, R. Pethig, J. Vykovákal and P. R. C. Gascoyne, *Proc. Natl. Acad. Sci.*, 1995, **92**, 860.

21 J. Cheng, E. L. Sheldon, L. Wu, A. Uribe, L. O. Gerrue, J. Carrino, M. J. Heller and J. P. O'Connell, *Nat. Biotechnol.*, 1998, **16**, 546.

22 T. Müller, G. Gradl, S. Howitz, S. Shirley, Th. Schnelle and G. Fuhr, *Biosens. Bioelectron.*, 1999, **14**, 247.

23 X. Hu, P. H. Bessette, J. Qian, C. D. Meinhart, P. S. Daugherty and H. T. Soh, *Proc. Natl. Acad. Sci. U.S.A.*, 2005, **102**, 15757.

24 P. C. H. Li and D. J. Harrison, *Anal. Chem.*, 1997, **69**, 1564.

25 I. Šafařík and M. Šafaříková, *J. Chromatography B*, 1999, **722**, 33.

26 V. I. Furdui and D. J. Harrison, *Lab Chip*, 2004, **4**, 614.

27 N. Pamme and C. Wilhelm, *Lab Chip*, 2006, **6**, 974.

28 Y. Zhou, Y. Wang and Q. Lin, *J. MEMS*, 2010, **19**, 743.

29 D. Robert, N. Pamme, H. Conjeaud, F. Gazeau, A. Iles and C. Wilhelm, *Lab Chip*, 2011, **11**, 1902.

30 T. Schneider, S. Karl, L. R. Moore, J. J. Chalmers, P. S. Williams and M. Zborowski, *Analyst*, 2010, **135**, 62.

31 M. Zborowski and J. J. Chalmers, *Anal. Chem.*, 2011, **83**, 8050.

32 X. Jin, S. Abbot, X. Zhang, L. Kang, V. Voskinarian-Berse, R. Zhao, M. V. Kameneva, L. R. Moore, J. J. Chalmers and M. Zborowski, *PLoS One*, 2012, **7**, e39491.

33 Y. Jung, Y. Choi, K.-H. Han and A. B. Frazier, *Biomed. Microdevices*, 2010, **12**, 637.

34 J. D. Adams, U. Kim and H. T. Soh, *Proc. Natl. Acad. Sci. U.S.A.*, 2008, **105**, 18165.

35 J. D. Adams, P. Thévoz, H. Bruus and H. T. Soh, *Appl. Phys. Lett.*, 2009, **95**, 254103.

36 H. Lee, J. Jung, S.-I. Han and K.-H. Han, *Lab Chip*, 2010, **10**, 2764.

37 B. B. Yellen, R. M. Erb, H. S. Son, R. Hewlin, Jr., H. Shang and G. U. Lee, *Lab Chip*, 2007, **7**, 1681.

38 G. Vieira, T. Henighan, A. Chen, A. J. Hauser, F. Y. Yang, J. J. Chalmers and R. Sooryakumar, *Phys. Rev. Lett.*, 2009, **103**, 128101.

39 T. Henighan, A. Chen, G. Vieira, A. J. Hauser, F. Y. Yang, J. J. Chalmers and R. Sooryakumar, *Biophys. J.*, 2010, **98**, 412.

40 E. Rapoport, D. Montana and G. S. D. Beach, *Lab Chip*, 2012, **12**, 4433.

41 A. R. Wheeler, W. R. Thronset, R. J. Whelan, A. M. Leach, R. N. Zare, Y. H. Liao, K. Farrell, I. D. Manger and A. Daridon, *Anal. Chem.*, 2003, **75**, 3581.

42 R. N. Zare and S. Kim, *Annu. Rev. Biomed. Eng.*, 2010, **12**, 187.

43 A. K. White, M. VanInsberghe, O. I. Petriv, M. Hamidi, D. Sikorski, M. A. Marra, J. Piret, S. Aparicio and C. L. Hansen, *Proc. Natl. Acad. Sci.*, 2011, **108**, 13999.

44 H. Song, D. L. Chen and R. F. Ismagilov, *Angew. Chem. Int. Ed.*, 2006, **45**, 7336.

45 S.-Y. Teh, R. Lin, L.-H. Hung and A. P. Lee, *Lab Chip*, 2008, **8**, 198.

46 S. Köster, F. E. Angilé, H. Duan, J. J. Agresti, A. Wintner, C. Schmitz, A. C. Rowat, C. A. Merten, D. Pisignano, A. D. Griffiths and D. A. Weitz, *Lab Chip*, 2008, **8**, 1110.

47 M. T. Guo, A. Rotem, J. A. Heyman and D. A. Weitz, *Lab Chip*, 2012, **12**, 2146.

48 E. Brouzes, M. Medkova, N. Savenelli, D. Marran, M. Twardowski, J. B. Hutchison, J. M. Rothberg, D. R. Link, N. Perrimon and M. L. Samuels, *Proc. Natl. Acad. Sci.*, 2009, **106**, 14195.

49 H. Zhang, G. Jenkins, Y. Zou, Z. Zhu and C. J. Yang, *Anal. Chem.*, 2012, **84**, 3599.

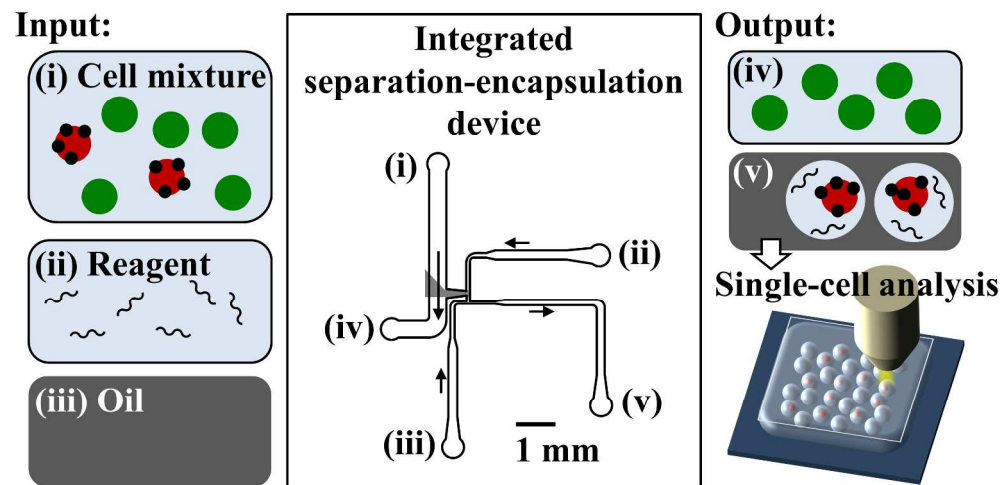
50 M. Chabert and J.-L. Viovy, *Proc. Natl. Acad. Sci.*, 2008, **105**, 3191.

51 E. Um, S.-G. Lee and J.-K. Park, *Appl. Phys. Lett.*, 2010, **97**, 153703.

52 S. Moon, U. A. Gurkan, J. Blander, W. W. Fawzi, S. Aboud, F. Mugus, D. R. Kuritzkes and U. Demirci, *PLoS One*, 2011, **6**, 8.

53 A. R. Abate, C.-H. Chen, J. J. Agresti and D. A. Weitz, *Lab Chip*, 2009, **9**, 2628.

54 E. W. M. Kemna, R. M. Schoeman, F. Wolbers, I. Vermes, D. A. Weitz and A. van den Berg, *Lab Chip*, 2012, **12**, 2881.



800x398mm (96 x 96 DPI)